

Heliotracking Device using Liquid Crystalline Elastomer Actuators

Hongye Guo, Mohand O. Saed, and Eugene M. Terentjev*

Many living organisms in nature respond to light stimulus and track the light source. Inspired by this, and to maximize the light-harvesting ability of solar cells, here, a spontaneous helio-tracking device based on the differential light-induced actuation of liquid crystalline elastomers (LCEs) is demonstrated.

The synthesis of the actuator material involves a robust thiol “click” polymerization, while the addition of indocyanine green (ICG) dye imparts the sensitivity to broad-spectrum and near-infrared light. Highly reproducible thermal and photo-induced linear actuation is demonstrated. The device is based on a freely pivoting payload platform held in place by several linear LCE actuators around the 360° circumference. The side of the device, which is exposed to light, has the actuators contracting and tilting the platform toward the light source. As the light source (e.g., the Sun) is moving around the device, the platform tilt followed, always exposing the payload face to the light; in the dark, the device recovers its neutral position.

achieved by the elongation of cells on the opposite side of the stem, away from sunlight. A similar mechanism of reversible elongation and contraction in response to light can be found in hydrogels^[2] and liquid crystalline elastomers,^[3,4] although systems using hydrogels often have a very long response time and are limited to only function in an aqueous environment.

Liquid crystalline elastomers (LCE) have been on the front of research and development for over 30 years, in part thanks to their remarkable actuation characteristics,^[5–7] but also due to their unique “soft elasticity” (development of mechanical strain without or with very low elastic resistance).^[8] The linear actuation of LCE can achieve a maximum strain of 500%^[9,10] and is fully reversible: the equilibrium length of an aligned LCE sample directly


reflecting the degree of the internal nematic order. Fundamentally, LCE actuation can be induced by any stimulus that affects the underlying nematic order in the polymer, and although the thermally induced phase change is the most natural phenomenon, the change in order can be triggered by other stimuli, such as light and magnetic field, when incorporating photo-absorbers^[3,4,11] or magnetic nano-particles.^[12] These properties make LCE a competitive material in practical applications ranging from soft robotics,^[13] to sensors,^[14] and smart textiles.^[15]

We have quite easily managed to mimic the phototropism of a sunflower, as illustrated in **Figure 1** (also see Movie S1, Supporting Information). By making a uniaxially aligned LCE cylinder with a photo-absorbing dye dispersed in the polymer network, we obtain the contraction in the side of this cylinder that is exposed to light, so that the cylinder bends toward the light source. The elastic modulus of the elastomer has to be sufficiently low so that the back side of the cylinder, which is shaded from light, allows the adequate extension. Importantly, such a “stalk” cannot bend too much: as soon as the face “overshoots,” the light falls on the back side of the cylinder and straightens it back. Figure 1b illustrates the kinetics of this bending, although the time depends on the cylinder dimensions and the material stiffness. Recently, such a freely-bending photo-tropic actuator has been reported by Qian et al.^[2] and by Yan et al.^[16] Bending actuation of LCEs is a well-studied phenomenon, especially when caused by photo-isomerization or photo-absorption, when an extended sample is illuminated from one side. This was utilized in various spectacular applications over the years^[17–21]. Unfortunately, as in Nature, such a bending filament cannot exert any significant force or do much mechanical work. Here

1. Introduction

Among all forms of renewable energy, solar energy has seen the biggest growth over the last decade and makes up 26% of renewable electricity generation in 2019.^[1] The majority of solar energy harvesting is achieved using solar panels, and their power output is heavily affected by the incident angle of light. As such, many solar farms utilize a combination of motors and computational algorithms to maintain a normal incidence on the panel face, at the cost of delicate engineering and additional energy input. An autonomous system that could operate without additional energy input would represent a high value in this field. In Nature, many living organisms possess the ability to move away or toward sources of light. Known as phototropism, this phenomenon often occurs in plants and fungi. Notoriously, sunflowers self-rotating to always face the sun, which is

H. Guo, Dr. M. O. Saed, Prof. E. M. Terentjev
Cavendish Laboratory
University of Cambridge
Cambridge CB3 0HE, U.K.
E-mail: emt1000@cam.ac.uk

 The ORCID identification number(s) for the author(s) of this article can be found under <https://doi.org/10.1002/admt.202100681>.

© 2021 The Authors. Advanced Materials Technologies published by Wiley-VCH GmbH. This is an open access article under the terms of the Creative Commons Attribution License, which permits use, distribution and reproduction in any medium, provided the original work is properly cited.

DOI: [10.1002/admt.202100681](https://doi.org/10.1002/admt.202100681)

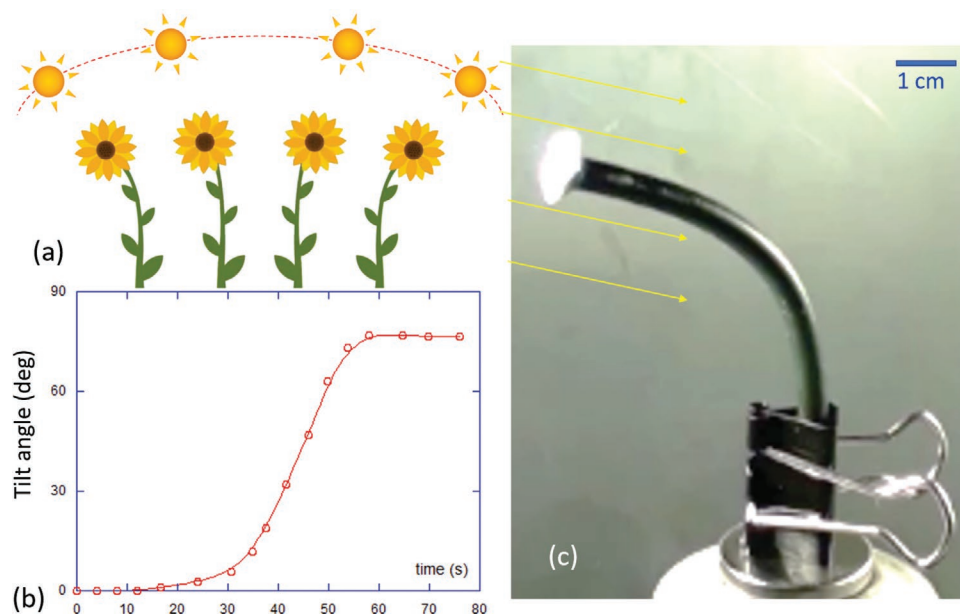


Figure 1. Illustration of phototropism in LCE. a) A sketch reminding of the sunflower principle. b) The response function of LCE filament, plotting the tilt angle versus time after the light is switched on. c) A filament of photo-sensitized LCE is shown to bend toward the light source, by contracting the side of the cylinder that faces the light (see Movie S1, Supporting Information).

we undertake two tasks to improve on this: to design a new actuating material, which will allow us to mold strong actuators in required shapes—and to engineer a heliotracking device that would be able to operate with a significant payload.

Our design, based on a tilting top platform moved by linear actuator contraction, is not dissimilar to another reported heliotracking system^[22]. However original, that work uses a very complicated LCE material processing and alignment, involving dispersion of polyurethane network and single-wall carbon nanotubes for photo-sensitivity, and a complex and delicate engineering, involving curved-mirror light concentrators—but no tension regulation. Our aim is to develop and present a practically useful heliotracking system, easy to produce, and robust in operation. For that reason we develop a simple and robust material, the cylindrical actuator shape that withstands significant tensile and compressive forces, and arrange them in a simple tilting-platform device with the strong pivot support that allows to adjust the actuator tension (and thus its range of response).

2. xLCE Actuator Material

The first viable LCE actuators were produced through hydrosilylation reaction of siloxane polymer backbone and vinyl or acrylate mesogens.^[5,23] The significant advance in the field has been achieved by utilizing the “click” chemistry of thiols, enabled by the commercial access to acrylate-terminated mesogens.^[24] Presently, a large variety of LCE materials are produced easily by non-specialist laboratories. The polydomain equilibrium state of LCE networks is always the outcome unless special alignment programming is used, as an inevitable result of the randomly quenched disorder in the crosslinked network of polymer chains.^[25] To program the aligned LCE configuration (called the “single crystal LCE” by Finkelmann in 1991^[26]) the network must

be uniaxially stretched to initiate the transition to monodomain nematic phase. The method of two-step crosslinking^[5,24,26] is widely used for permanent LCE alignment, which gives a large uniaxial anisotropy in equilibrium and a large unidirectional actuation stroke as a consequence. However, this method does not work well when programming more complex structures other than flat films or thin cylinders: the fundamental concept of two-step crosslinking is that alignment must be forced before the final crosslinking step. The competing demands of alignment (which requires low crosslinking density) and the first step network crosslinking (which is needed for sample integrity) unavoidably limits the LCE produced this way. Other alignment techniques, such as surface alignment^[27] and shear-extrusion alignment,^[9] exist but are also limited due to similar causes.

One breakthrough has occurred recently when the concept of “vitrimers” was introduced by Leibler et al.^[28] Unlike conventional covalently crosslinked thermosets, vitrimers have a polymer network containing molecular groups capable of bond exchange reactions (BER), and the initiation of BER under stress can alter their internal topology.^[29] Today, there are many examples of such generic dynamic covalent chemistry, which in all cases enables programming after full cross-linking by activating the BER. In the context of “exchangeable LCE” (xLCE)^[30] this mitigates the competition between alignment and crosslinking and makes molding complex geometries possible—as well as the recycling through thermal remolding.^[31]

One particular bond-exchange mechanism is important for the present work. By using the highly flexible Si-O linkages within the network can significantly lower the glass transition point (T_g), while maintaining exceptional mechanical properties.^[32] The equilibrium exchange in the siloxane adaptable networks^[33–35] is an established BER mechanism. Here we further develop the siloxane-based xLCE system,^[36] adapting it for the broad-spectrum photo-actuation applications, and

develop a prototype heliotracking device with artificial phototropism enabled by an assembly of xLCE actuators. To enable the light-induced actuation, a fluorescent dye indocyanine green (ICG) is evenly dispersed inside the material: it acts as an efficient light absorber and provides the photo-thermal energy conversion for the nematic-isotropic phase transition and actuation of xLCE.

3. xLCE Material Characterization

The traditional way to characterize phase transformation in LCE materials is by differential calorimetry, which normally shows the thermal glass transition as a step in the scan, and the first order nematic-isotropic transition as a heat capacity peak, the area under which represents the latent heat of the transition. It is not clear to us why this particular material, combining siloxane-ring crosslinkers, as in ref. [36], and a fraction of siloxane spacers, as in ref. [37], does not show any noticeable nematic transition peak. It could be because of the excessive internal sources of quenched disorder (caused by nano-scale attempt to de-mix siloxane from the rest of the polymer) makes the transition to become more continuous,^[38,39] or for some other reason. This is not uncommon in siloxane-containing main-chain LCE. There is no doubt that a nematic isotropic transition takes place, which is apparent in the sample appearance as well as in the actuation data below. However, failing differential calorimetry, we had to use dynamic-mechanical trace to identify the transitions in a polydomain xLCE through heating at a constant frequency of 1 Hz, **Figure 2a**.

The dynamic glass transition T_g is identified around $-5\text{ }^\circ\text{C}$ as the peak of the characteristic loss peak in $\tan\delta$. Fundamentally, it is not the same as the thermal glass transition in a stress-free sample, but at low frequency and strain amplitude we expect the two to be close. The nematic-isotropic phase transition is found near T_{NI} around $60\text{ }^\circ\text{C}$, indicated by the characteristic drop in the modulus because of “dynamic soft elasticity.”^[40,41]

To test the relation between BER rate and temperature, an iso-stress temperature ramp experiment was carried out as

shown in **Figure 2b**. The elastomer deforms strictly at constant volume, and what we are exploring is the uniaxial nematic contraction followed by the elastic-plastic transition. There are three stages in the test, involving stress ramping, strain equilibration, and then the temperature ramp at fixed load. A stress was first applied (at a fast rate of 50 kPa min^{-1}) to the polydomain xLCE at $30\text{ }^\circ\text{C}$, resulting in a strain of 37% when the stress reached the final value of 50 kPa. The sample was then allowed to relax at the same temperature and fixed load for 20 min, which resulted in a small relaxation of strain (further elongation). It is important to recognize that this extension is purely mechanical as the nematic order remains constant at the first two stages of this test; also the temperature was too low for the onset of any plastic creep due to bond exchange. The slow relaxation in polydomain LCE, however, is a known feature of these materials.^[42] This initial extension is achieved by the deformation and rotation of locally uniaxial domains driven by the uniaxial applied stress, which is different to the actuation of a programmed uniaxial material due to isotropic-nematic phase transition. Maintaining the stress at this relatively low value of 50 kPa, the sample was then heated with a heating rate of $2\text{ }^\circ\text{C min}^{-1}$. Upon heating, the sample first contracted as it changed from the stress-aligned nematic to isotropic, followed by a further decrease of strain in the isotropic phase (the classical rubber-elastic effect of entropic modulus increasing with temperature). At around $100\text{ }^\circ\text{C}$, the gradient of the plot reaches zero, indicating that plastic flow due to BER had overtaken the entropic effect of contraction.^[43] The rate of plastic creep increases with temperature, and the sample eventually reached the fast-flow regime above $250\text{ }^\circ\text{C}$.

To further understand the effect of temperature on the BER rate, xLCE programming at three different temperatures was carried out, **Figure 3a**. The sample was first heated up to the designated temperature, at which a noticeable bond exchange should take place, with no stress applied, followed by a stress ramp (50 kPa min^{-1}) reaching the fixed value of 100 kPa. The plastic creep of the sample at constant stress and temperature was monitored, and the experiments were terminated after reaching over 100% strain. At this degree of uniaxial creep,

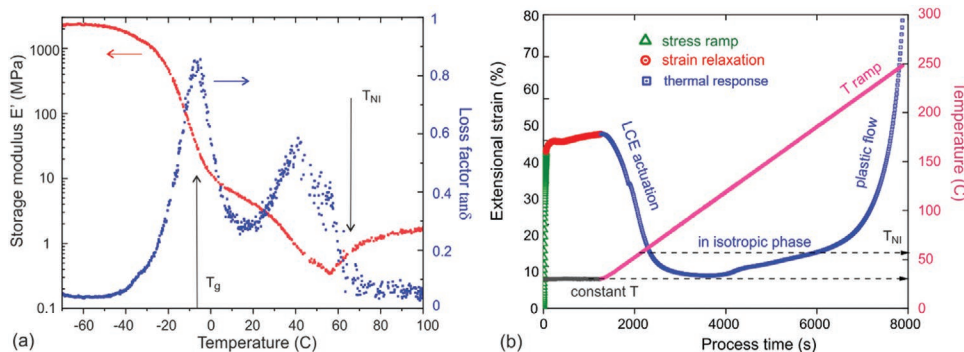


Figure 2. a) Dynamic mechanical analysis of xLCE: the linear storage modulus E' and the loss factor $\tan\delta$ measured at a constant frequency of 1 Hz, are plotted against temperature. The glass transition temperature T_g was determined by the first peak in $\tan\delta$ at $T_g = -5\text{ }^\circ\text{C}$. The nematic-isotropic transition temperature T_{NI} was determined by the characteristic drop in modulus at $T_{NI} = 60\text{ }^\circ\text{C}$. Note that at these temperatures, no BER is expected, and the material behaves as full thermoset. b) Iso-stress temperature ramp curve shows how the strain changes with temperature, while maintaining a constant stress of 50 kPa. After the initial stress ramp and equilibration that occur at a constant $T = 30\text{ }^\circ\text{C}$, the strain on the temperature ramp changes in three distinct stages representing: the LCE actuation (contraction at T_{NI}), the classical effect of entropic elasticity (increase in rubber modulus as temperature rises), and the increasing plastic flow due to the bond-exchange. The onset of plastic flow occurs at around $100\text{ }^\circ\text{C}$, with the network in “free-flow” near $250\text{ }^\circ\text{C}$.

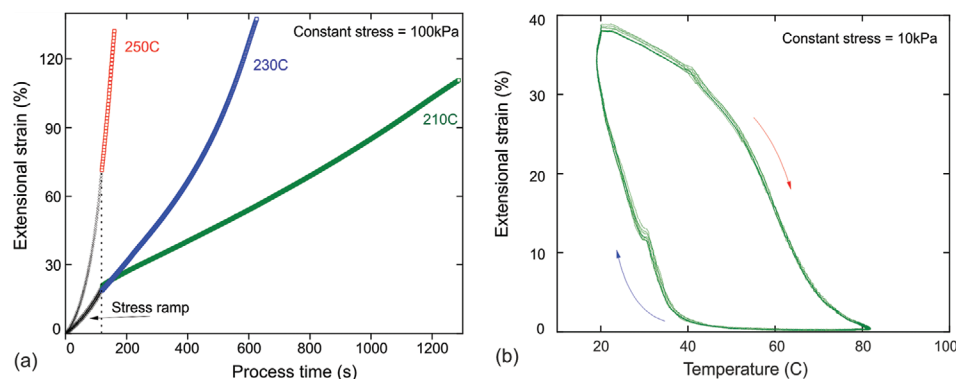


Figure 3. a) Programming of the aligned monodomain in xLCE: After equilibrating at a fixed (high) temperature (labeled in the graph), and a quick a stress ramp, the samples were kept under a constant tensile stress of 100 kPa to monitor their plastic creep. The samples were allowed to flow to over 100% extension, reaching a sufficient uniaxial anisotropy in the rearranging network, and on cooling have retained the monodomain alignment. The rate of BER increases significantly at higher temperatures, and the 250 °C sample reached 100% strain in under a minute. b) 10 cycles of contraction-extension on repeated heating and cooling. The extension strain is plotted against temperature, showing the reproducibility of linear actuation and the extent of thermal hysteresis at the heating rate of 5 °C min⁻¹. A constant tensile stress of 10 kPa was applied during the test to keep the sample straight and taut.

the samples were recognized as sufficiently programmed for uniaxial monodomain alignment, which was fully retained on their cooling to the nematic phase. It is apparent from the plot that BER rate is heavily affected by the temperature, and a high temperature will provide the most efficient programming. BER can be modeled as a classical thermally activated effect with the rate: $k = \omega_0 \cdot e^{-\Delta G/k_B T}$, where ω_0 is the ‘rate of attempts’ (which itself is a function of temperature) and ΔG represents the activation energy barrier (measured as ≈ 116 kJ mol⁻¹ by Saed et al.^[36]). It was important for our device operation that while the nematic-isotropic phase change, leading to linear actuation, occurs below 60–80 °C, no plastic creep took place at those temperatures, so the established programming could be retained.

With the sample programmed to achieve uniaxial monodomain, its thermal actuation behavior was examined through repeated cycles of heating and cooling through its nematic-isotropic phase transition. Figure 3b shows the reversible actuation under a low stress of 10 kPa to keep the sample straight. The test was carried out between 20 and 80 °C which covers the working temperature it would experience in the heliotracking device. On heating, the sample started to rapidly contract around 50 before reaching its saturation strain when the temperature approached 80 °C. On cooling, the cycles reversed, and the sample started to expand quickly after dropping below 40 °C. A total of ten cycles are shown in the graph, overlapping each other almost perfectly. For the ease of demonstration, the 0% strain is the reference in the material’s isotropic phase.

4. Heliotracker Design

Phototropic bending (illustrated in Figure 1) is not useful for a practical device, as it cannot support any meaningful payload. Attempts could be made to somewhat increase the mechanical load bearing capacity of such a system, as has been demonstrated by Yan et al.^[16] Instead, we have designed a device that works on linear contraction of xLCE actuator, and as a result, could generate significant mechanical work. Figure 4 illustrates

xLCE actuation under high tension in a device where the specially designed “dog bone” actuator is set in series with a linear spring, to allow easy control of the tension applied (see Movie S2, Supporting Information). The rounded edges of the actuator caps allow for the firm grip by a variety of devices, while not leading to sharp stress concentrations that invariably result in cracking under high load. The actuation under tension of 5 N implies lifting the weight of about 500 g by such a device, with many repetitions without failure. The dimensions and the xLCE material used started to show failure on actuation against the resisting load above 8 N, that is, the tensile stress of 0.29 MPa. It is interesting, and encouraging, that our estimate of the maximum mechanical work extracted from the actuator, in the geometry shown in Figure 4d, was of the order $\Delta W \approx 0.17\text{--}0.2$ J g⁻¹, which is close to the latent heat of the nematic-isotropic transition (as reported in many calorimetry studies of LCE). This means that most of the free energy stored in the nematic order in our actuator is being converted into mechanical energy stored in the spring. In turn, this means that this is the order of mechanical energy one could extract in a well-designed actuating device, like the one we discuss below.

The heliotracker consists of two parallel platforms connected by eight specially shaped xLCE linear actuators placed around their circumference. The top platform is made freely pivoting. Upon illumination from one side, the actuators near the light source contract and tilt the top “payload” platform to face the light source. The tilt of the payload face rotates around the 360° circumference as the light source moves around it. When the light is turned off, the platform quickly returns to its natural flat configuration being pulled back by the stretched xLCE segments. We first discuss the material production and its characteristics, before going into details of heliotracking design, and its operation.

Figure 5 illustrates the principles of the design, which combine several requirements. The xLCE actuators are located around the circumference of this device, and when light illuminates from the side, the actuators facing the light will contract, and tilt the top platform so that it always tracks the light source

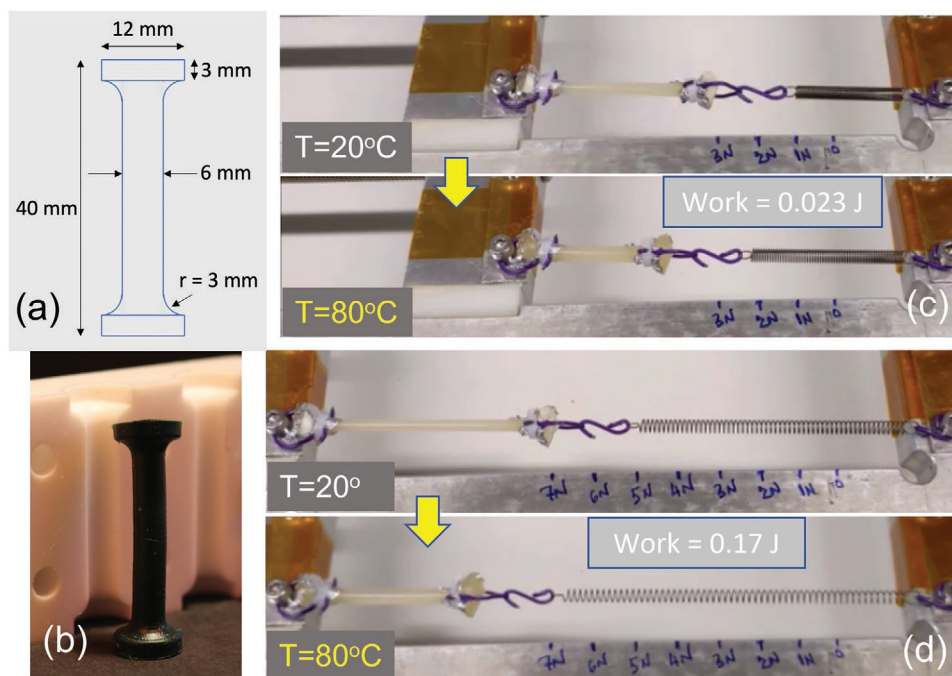


Figure 4. LCE actuation under high load. a) The design of the “dog bone” actuator mold to fit into the heliotracker slots, highlighting the rounded edges of the caps. b) The xLCE actuator shown standing next to its mold. Note the deep color of the elastomer, which is due to the broad-spectrum absorbance of ICG. c) The “dog bone” actuator was mounted in series with a spring in a length-controlled device, having the spring stretched to a tension of 1 N at ambient temperature. On heating to isotropic phase, the actuator contracts reaching a tension of 2.1 N, and producing mechanical work of 0.023 J. d) The same in-series device stretches the spring to a tension of 5 N, which rises to 6.7 N on actuation, with the work of 0.15 J stored in the spring (see Movie S2, Supporting Information).

(and achieve better energy conversion efficiency if loaded with a solar cell). So, a key requirement was the free tilting of the top plate. The other requirement, which we found very important, is that the contact between the elastomer actuator (often at high stress during the device operation) and solid parts must be smooth and not induce stress concentration, which would quickly end up in fracturing the elastomer.

The device is designed to have its height adjustable by connecting the top and bottom plates with a long steel screw. This was incorporated into the design to enable different pretension on elastomer struts, as it is known that both the actuation and the tensile stress are non-linear functions of pre-tension, and optimization of this would improve the performance. A nut is

threaded onto the screw in between the two plates to secure the chosen height adjustment. To enable the tilting motion of the top plate in every direction, the end of the screw is tapered with a hemispherical tip, and the center of the bottom side of the top plate is indented, effectively acting as a spherical cap for the tip. This design feature also allows a heavy payload weight balancing on the top platform without any effect on the actuation performance. Instead of metal, polyether ether ketone (PEEK) is chosen as the material for the plates as it has a low density, low heat conductivity, high temperature tolerance and is relatively soft, thus easy to machine.

Cylindrical geometry was selected for the body of xLCE actuators as it ensures equal illumination at all angles, with

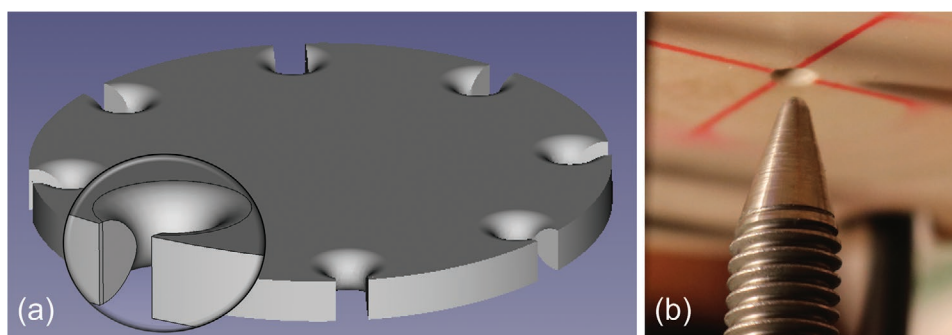


Figure 5. Design of the heliotracking device. a) The CAD model of the top and bottom plates. One of the eight slots is magnified to highlight the rounded edges, essential for the actuator grasp, but not initiating stress concentrations. b) The connecting mechanism of the central screw and the top plate, which allows a free pivot of the top plate, and the high payload on the top plate supported.

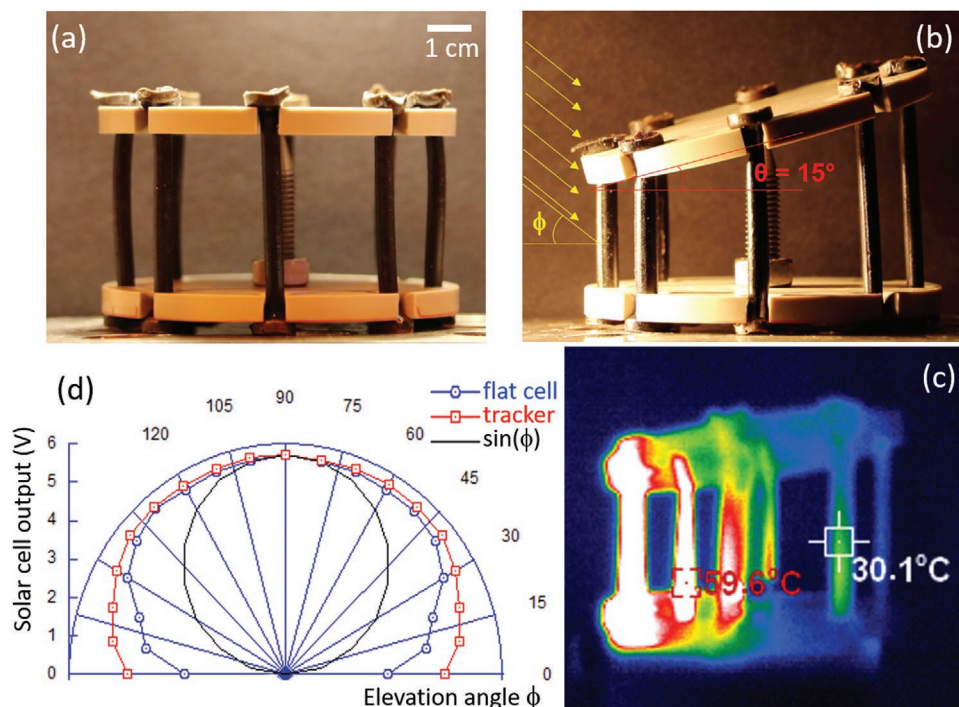


Figure 6. The heliotracker in action. a) Before the illumination, the device was at a neutral position at ambient temperature. b) After 100 s of illumination, the device reached its equilibrium state, exhibiting a tilting angle of 15° (see Movie S3, Supporting Information). c) The thermal image under illumination indicates that the exposed actuators have reached the temperature of 60°C , sufficient to initiate contraction, while those at the back are stretching at ambient temperature. d) Polar plot of measured solar cell output, with the light source scanning the full 180° arc angle ϕ , comparing the fixed flat cell and the cell mounted on heliotracker.

carefully designed rounded caps to eliminate stress concentration corners. To attach the actuators to the platforms, they were designed such that the actuators can be slotted into the platforms and mechanically locked in place, yet easy to replace if needed.

5. Heliotracker Actuation

After slotting the eight actuators into the device, and adjusting the height of the supporting screw for the chosen pre-tension, the fully assembled heliotracker was tested with the laboratory light source, used to imitate the Sun: illuminating light and radiating heat with a black-body radiation spectrum at a chosen temperature. The response to illumination from one side is shown in Figure 6 (also see Movie S3, Supporting Information). Actuators facing the lamp (front side) were heating up gradually, due to the strong high heat release from photo-absorbing ICG dye, and started to contract as the temperature approached the nematic–isotropic transition T_{NI} . This resulted in significant tilting of the top platform, which is turning to face the lamp. Actuators on the back side were stretched because of the tilting motion but were shielded from the light/heat by the tilted platform. The equilibrium state was established within about 100 s, when the temperature profile stabilized and the tension in the front and back side actuators balanced each other. Once the lamp was turned off, the contracted actuators cooled down and changed from isotropic back to nematic phase. With this, the top platform recovered to its initial position (horizontal)

driven by the tension in the back actuators. We found that such a “forced” recovery took about 120 s. In the steady state, the tilting angle θ reached a maximum of 15° , but a higher tilting angle is easily achievable by changing the dimension of the top and bottom plates.

The polar plot in Figure 6d shows the measurement of a solar cell output, for the light source travelling along the full arc of elevation angle ϕ . Here we compare the output of a fixed planar cell, which as expected has the maximum output at the 90° light elevation, with the same cell mounted on the payload platform of heliotracker. The reason neither test gives zero output at zero elevation (as the geometry of light flux would suggest) is the ambient scattering of light in the testing chamber. However, the effect of heliotracking is plain to see: the platform tilts to track the light source and its output at increasingly oblique angles is significantly higher. The total area under the heliotracking (red) curve is 9% higher than that under the fixed-cell (blue) curve, which is a crude measure of the gain in total energy output

6. Conclusion

In summary, we have designed and built a prototype heliotracking device that can track the light source autonomously using the intrinsic differential actuation of xLCE material. The heliotracking by bending mimics closely the sunflower face following the Sun, however, we focused on an engineering design that could support a useful heavy payload. To this end,

we investigated the limits of linear tension, mechanical work, and the strength to break of the specially designed actuator shape that optimizes these parameters. In our heliotracker, linearly-contracting actuators are evenly distributed around the circumference, and impart the tilting motion of the payload platform. The xLCE material was synthesized through sequential thiol-ene and thiol-acrylate Michael addition click reactions, ensuring a robust material with high reproducibility of actuation. The photo-sensitivity was imparted by using the ICG dye, which is commonly used in plastic welding and in therapy due to its high photo-thermal conversion efficiency. The heliotracker device relies on the specially-shaped actuator struts, which were designed to be replaceable in the device. It was essential for us to be using the exchangeable xLCE to be able to produce such actuators and program their uniaxial alignment. The freely pivoting payload platform of the device is shown to quickly tilt toward the source of illumination, achieving 15° angle in our demonstrator, and quickly recover to its neutral position when the light source is removed. This ensures that the platform tilt is easily following the light source as it travels around the device at the diurnal rate. This suggests a promising application of helio-tracking solar panels, theoretically increasing the power generation by over 10%. For countries with a big solar energy capacity, like China with an average 130 GW, the application of helio-tracking solar panels could bring significant benefits.

7. Experimental Section

Materials: Di-acrylate liquid crystal (LC) mesogen RM82 was purchased from Daken Chemical Co. Di-thiol spacer 2,2'-ethylenedioxy)diethanethiol

(EDDT), di-vinyl siloxane spacer 1,3-divinyltetramethyldisiloxane (DVTS) and tetra-vinyl siloxane cross-linker 2,4,6,8-tetramethyl-2,4,6,8-tetravinylcyclotetrasiloxane (TVTS) were purchased from Sigma-Aldrich. The photo-initiator, Irgacure I-651 was purchased from Sigma-Aldrich. 4-dimethylaminopyridine (DMAP) and triphenylphosphine (PPh₃) were purchased from Sigma-Aldrich and used as the catalyst for thiol-acrylate Michael addition reaction and siloxane equilibrium bond exchange reaction respectively. Toluene and dimethylformamide (DMF) were purchased from Sigma-Aldrich and used as solvent. The photo-absorber Indocyanine green (ICG) was purchased from Tokyo Chemical Industry Co.

Synthesis of xLCE Actuators: For this work, due to the presence of photo-absorber ICG in the final elastomer actuator, the synthesis process had to be revised to avoid using the actual "UV crosslinking"^[36] at the late stage when ICG was involved. Instead, the first step was to prepare multi-functional oligomers by UV-initiated reaction that converts all the crosslinkers, and then add ICG and the mesogenic components into the reacting mixture for the thermally activated thiol-acrylate reaction that links together the network of multi-functional oligomers.

xLCE actuators were synthesized in two steps via two variants of the thiol-ene reaction. In one container, the tetra-vinyl siloxane cross-linker TVTS (0.5mmol) and the di-vinyl siloxane spacer DVTS (1 mmol) were mixed with excess amount of di-thiol spacer EDDT (7 mmol). Thiol-ene reaction via free-radical addition proceeded in the presence of i-651 photoinitiator (1.5 wt%) and 60 min of 365 nm UV irradiation. In a separate container, photoabsorber ICG (0.5 wt%), DMAP (0.5 wt%) and PPh₃ catalyst (2 wt%) were dissolved in a small amount of DMF (4 wt%) before adding toluene (40 wt%). Contents in both containers were combined, and the reacting mesogen RM82 (5 mmol) was added and dissolved, assisted by heating and vigorous mixing using a Vortex mixer. Air bubbles were removed under vacuum. The solution was injected into the custom-made mold, confer Figure 4d, and allowed to cure at room temperature overnight via the thiol-acrylate Michael addition reaction. Solvent removal was achieved by placing the actuators in a vacuum oven at 80 °C for 24 h. The details of the reaction scheme are shown in **Figure 7**.

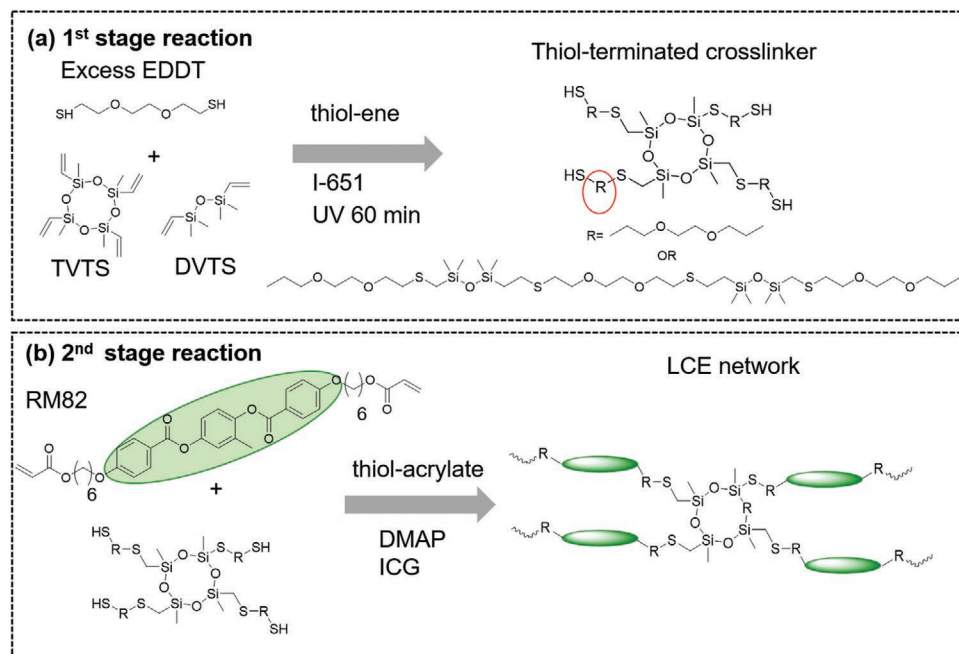


Figure 7. Chemical synthesis route for the photo-sensitized xLCE material. a) The siloxane species (the spacer DVTS and the crosslinker TVTS) first react with the excess amount of di-thiol (EDDT) under UV to form thiol-terminated oligomers. b) The resulted siloxane-crosslinked oligomers and the remaining EDDT are mixed with RM82 acrylate mesogens, with ICG dye added at this stage so that it would not affect the thiol-acrylate Michael addition to form the final LC polymer network. The exchangeable siloxane segments are found in the crosslinkers, and in the extended linear spacers marked by **R** in the schemes.

Design of the Mold: The xLCE polymerization and crosslinking were carried out in a custom-made mold cut out in a block of Teflon. The design of this mold has been optimized in several stages, to ensure the xLCE actuators were produced in the required dimensions, and were equipped with special features (such as rounded corners and bulky top) to evenly distribute the stress and avoid fracture even at very high deformations. The CAD designs were produced, and used in a computer numerical controlled (CNC) machine in the Cavendish Workshop to produce the mold.

Dynamic Mechanical Analysis: Dynamic mechanical analysis was performed on a TA instrument Discovery 850 in tensile mode. A strip-shaped sample cut from a thin film with a cross-section of $0.6 \times 3.5 \text{ mm}^2$ was used for this characterization. The sample was cycled at 1 Hz with a strain amplitude of 0.01% and heated from -70 to $100 \text{ }^\circ\text{C}$ at a rate of $4 \text{ }^\circ\text{C min}^{-1}$.

Strain Actuation Cycles: The test was performed using the same TA Discovery 850 instrument in tensile mode. A strip-shaped sample cut from a thin film with a cross-section of $0.6 \times 3.5 \text{ mm}^2$ was used for the measurement. The starting length (at room temperature) was measured. The sample was equilibrated at $30 \text{ }^\circ\text{C}$ after which a constant stress of 100 kPa was applied. The sample then went through 10 cycles of heating and cooling between 20 and $80 \text{ }^\circ\text{C}$ with a soak time of 5 and 10 min after heating and cooling, respectively. The heating and cooling rate was $5 \text{ }^\circ\text{C min}^{-1}$. The associated change in sample length (at constant stress) was recorded and presented as actuation stroke.

Iso-Stress Temperature Ramp: The test was performed using the same TA Discovery 850 instrument in tensile mode. A strip-shaped sample cut from a thin film with a cross-section of $0.6 \times 3.5 \text{ mm}^2$ was used for the measurement. The starting length (at room temperature) was measured. The sample was equilibrated at $30 \text{ }^\circ\text{C}$ and quickly stretched (at a rate of 50 kPa min^{-1}) until the stress reached 50 kPa. After that sample was allowed to creep under constant stress for 20 min for equilibration, after which the heating ramp was applied at $2 \text{ }^\circ\text{C min}^{-1}$ until reaching $250 \text{ }^\circ\text{C}$. The length of the sample at constant stress was monitored and presented—this measurement combines the effects of LCE actuation (contraction on heating at constant stress) and the plastic flow due to bond exchange activated at high temperatures.

Programming of Aligned Actuators: Programming procedure to produce uniaxial alignment of demonstrator xLCE samples was first established using the same TA Discovery 850 instrument in tensile mode. Strip-shaped samples cut from a thin film with a cross-section of $0.6 \times 3.5 \text{ mm}^2$ were used. The samples were equilibrated at a high temperature above the elastic-plastic transition, then a medium level stress was applied to each sample, and they were allowed to creep until reaching 100% extension strain. This was the criterion for “standard” full alignment of xLCE.^[36]

The molded heliotracker actuators were programmed following the protocol established above, in an oven, using clamps and constant weight, at a slightly lower temperature (the detailed discussion in the text below) in order to avoid evaporation of the ICG dye. Because of that, the time under constant load in the oven was much longer (4 h), using the same criterion of 100% creep extension.

Model Light Sources: To mimic the sunlight, the Schott KL1500 LCD light source that produces the black-body radiation spectrum with a peak at $T = 3200 \text{ K}$ was used, and the Phillips incandescent R125 (300 W) lamp that produces a broad white light was also used. The intensity of broad-spectrum light was difficult to measure unambiguously. To try to stay as close to the real sunlight as possible, the solar cells were taken outside on a bright day, registering the photo-voltage (5.5–6 V) and then adjusting the distance to the lab light source until the 90° illumination of the same solar cell would give the same photo-voltage.

Solar Cell Output Measurement: To measure a practical benefit of heliotracking in the solar cell output, two standard commercial solar cells were used: SunPower Mini 1.8 W cell (from MPow) and RS Pro 1.5 W cell (from RS Online); Figure 6d shows the SunPower result illuminated with the Phillips R125 lamp mounted on a swivel to vary the illumination angle, while maintaining the fixed distance of 30 cm to the center of the cell. The voltage output of the cell was recorded for data analysis.

Supporting Information

Supporting Information is available from the Wiley Online Library or from the author.

Acknowledgements

This work has been supported by the ERC (Horizon 2020) Advanced grant 786659, and by the Chinese Scholarship Council. The help and advice of Alexandra Gablier in the polymer chemistry, and of the Cavendish Workshop in designing and manufacturing the device is gratefully acknowledged.

Conflict of Interest

The authors declare no conflict of interest.

Data Availability Statement

The data that support the findings of this study are available from the corresponding author upon reasonable request.

Keywords

heliotracking, liquid crystalline elastomers, photo-actuation

Received: June 7, 2021

Revised: June 11, 2021

Published online:

- [1] bp p.l.c., Statistical Review of World Energy, <https://www.bp.com/content/dam/bp/business-sites/en/global/corporate/pdfs/energy-economics/statistical-review/bp-stats-review-2019-full-report.pdf> (accessed: 2019).
- [2] X. Qian, Y. Zhao, Y. Alsaïd, X. Wang, M. Hua, T. Galy, H. Gopalakrishna, Y. Yang, J. Cui, N. Liu, M. Marszewski, L. Pilon, H. Jiang, X. He, *Nat. Nanotechnol.* **2019**, *14*, 1048.
- [3] P. M. Hogan, A. R. Tajbakhsh, E. M. Terentjev, *Phys. Rev. E* **2002**, *65*, 041720.
- [4] J. E. Marshall, E. M. Terentjev, *Soft Matter* **2013**, *9*, 8547.
- [5] J. Küpfer, H. Finkelmann, *Macromol. Chem. Phys.* **1994**, *195*, 1353.
- [6] A. R. Tajbakhsh, E. M. Terentjev, *Eur. Phys. J. E* **2001**, *6*, 181.
- [7] M. Warner, *Annu. Rev. Condens. Matter Phys.* **2020**, *11*, 125.
- [8] M. Warner, P. Bladon, E. Terentjev, *J. Phys. II France* **1994**, *4*, 93.
- [9] S. Ahir, A. Tajbakhsh, E. Terentjev, *Adv. Funct. Mater.* **2006**, *16*, 556.
- [10] M. O. Saed, R. H. Volpe, N. A. Traugott, R. Visvanathan, N. A. Clark, C. M. Yakacki, *Soft Matter* **2017**, *13*, 7537.
- [11] T. White, D. J. Broer, *Nat. Mater.* **2015**, *14*, 1087.
- [12] S. Herrera-Posada, C. Mora-Navarro, P. Ortiz-Bermudez, M. Torres-Lugo, K. M. McElhinny, P. G. Evans, B. O. Calcagno, A. Acevedo, *Mater. Sci. Eng. C* **2016**, *65*, 369.
- [13] A. Kotikyan, C. McMahan, E. C. Davidson, J. M. Muhammad, R. D. Weeks, C. Daraio, J. A. Lewis, *Sci. Robot.* **2019**, *4*, eaax7044.
- [14] C. Ohm, M. Brehmer, R. Zentel, *Adv. Mater.* **2010**, *22*, 3366.
- [15] T. Ohzono, M. O. Saed, Y. Yue, Y. Norikane, E. M. Terentjev, *Adv. Mater. Interfaces* **2020**, *7*, 1901996.
- [16] Y. Yan, Y. Zhao, Y. Alsaïd, B. Yao, Y. Zhang, S. Wu, X. He, *Adv. Intell. Syst.* **2021**, 2000234, <https://doi.org/10.1002/aisy.202000234>.

- [17] N. Tabiryán, S. Serak, X.-M. Dai, T. Bunning, *Opt. Express* **2005**, *13*, 7442.
- [18] K. K. Hon, D. Corbett, E. M. Terentjev, *Eur. Phys. J. E* **2008**, *25*, 83.
- [19] T. J. White, N. V. Tabiryán, S. V. Serak, U. A. Hrozhyk, V. P. Tondiglia, H. Koerner, R. A. Vaia, T. J. Bunning, *Soft Matter* **2008**, *4*, 1796.
- [20] C. van Oosten, C. Bastiaansen, D. Broer, *Nat. Mater.* **2009**, *8*, 677.
- [21] C. van Oosten, C. Bastiaansen, D. Broer, *Nat. Commun.* **2017**, *8*, 15546.
- [22] C. Li, Y. Liu, X. Huang, H. Jiang, *Adv. Func. Mater.* **2012**, *22*, 5166.
- [23] H. Finkelmann, H.-J. Kock, G. Rehage, *Makromol. Chem. Rapid Commun.* **1981**, *2*, 317.
- [24] C. M. Yakacki, M. Saed, D. P. Nair, T. Gong, S. M. Reed, C. N. Bowman, *RSC Adv.* **2015**, *5*, 18997.
- [25] S. V. Fridrikh, E. M. Terentjev, *Phys. Rev. E* **1999**, *60*, 1847.
- [26] J. Küpfer, H. Finkelmann, *Makromol. Chem., Rapid Commun* **1991**, *12*, 717.
- [27] T. H. Ware, M. E. McConney, J. J. Wie, V. P. Tondiglia, T. J. White, *Science* **2015**, *190*, 982.
- [28] D. Montarnal, M. Capelot, F. Tournilhac, L. Leibler, *Science* **2011**, *334*, 965.
- [29] M. McBride, B. Worrell, T. Brown, L. Cox, N. Sowan, C. Wang, M. Podgorski, A. Martinez, C. Bowman, *Annu. Rev. Chem. Biomol. Eng.* **2019**, *10*, 175.
- [30] Z. Pei, Y. Yang, Q. Chen, E. M. Terentjev, Y. Wei, Y. Ji, *Nat. Mater.* **2014**, *13*, 36.
- [31] M. O. Saed, A. Gablier, E. M. Terentjev, *Chem. Rev.* **2021**, <https://doi.org/10.1021/acs.chemrev.0c01057>.
- [32] B. H. Jo, L. M. Van Lerberghe, K. M. Motsegood, D. J. Beebe, *J. Microelectromech. Syst.* **2000**, *9*, 76.
- [33] R. C. Osthoff, A. M. Bueche, W. T. Grubb, *J. Am. Chem. Soc.* **1954**, *76*, 4659.
- [34] S. W. Kantor, W. T. Grubb, R. C. Osthoff, *J. Am. Chem. Soc.* **1954**, *76*, 5190.
- [35] P. Zheng, T. J. McCarthy, *J. Am. Chem. Soc.* **2012**, *134*, 2024.
- [36] M. O. Saed, E. M. Terentjev, *Sci. Rep.* **2020**, *10*, 6609.
- [37] Y. Wu, Y. Yang, X. Qian, Q. Chen, Y. Wei, Y. Ji, *Angew. Chem., Int. Ed.* **2020**, *59*, 4778.
- [38] L. Petridis, E. M. Terentjev, *Phys. Rev. E* **2006**, *74*, 5.
- [39] G. Cordoyiannis, A. Lebar, B. Zalar, S. Zumer, H. Finkelmann, Z. Kutnjak, *Phys. Rev. Lett.* **2007**, *99*, 197801.
- [40] A. Hotta, E. M. Terentjev, *Eur. Phys. J. E* **2003**, *10*, 291.
- [41] S. M. Clarke, A. R. Tajbakhsh, E. M. Terentjev, M. Warner, *Phys. Rev. Lett.* **2001**, *86*, 4044.
- [42] S. M. Clarke, E. M. Terentjev, *Phys. Rev. Lett.* **1998**, *81*, 4436.
- [43] R. H. Pritchard, A.-L. Redmann, Z. Pei, Y. Ji, E. M. Terentjev, *Polymer* **2016**, *95*, 45.